

SCIENTIFIC REPORTS



OPEN

Interrogation of γ -tubulin alleles using high-resolution fitness measurements reveals a distinct cytoplasmic function in spindle alignment

Kristian Shulist, Eric Yen, Susanne Kaitna, Allen Leary, Alexandra Decterov, Debarun Gupta & Jackie Vogel

γ -Tubulin has a well-established role in nucleating the assembly of microtubules, yet how phosphorylation regulates its activity remains unclear. Here, we use a time-resolved, fitness-based SGA approach to compare two γ -tubulin alleles, and find that the genetic interaction profile of γ tub-Y362E is enriched in spindle positioning and cell polarity genes relative to that of γ tub-Y445D, which is enriched in genes involved in spindle assembly and stability. In γ tub-Y362E cells, we find a defect in spindle alignment and an increase in the number of astral microtubules at both spindle poles. Our results suggest that the γ tub-Y362E allele is a separation-of-function mutation that reveals a role for γ -tubulin phospho-regulation in spindle alignment. We propose that phosphorylation of the evolutionarily conserved Y362 residue of budding yeast γ -tubulin contributes to regulating the number of astral microtubules associated with spindle poles, and promoting efficient pre-anaphase spindle alignment.

γ -Tubulin is an evolutionarily conserved member of the tubulin superfamily^{1,2} whose essential function is the nucleation of microtubules (MTs) in eukaryotic cells²⁻⁷. In budding yeast, γ -tubulin is encoded by the essential gene *TUB4*⁸. γ -Tubulin, Spc97 and Spc98 form γ -tubulin complexes (γ TuCs) located on the nuclear and cytoplasmic surfaces of spindle pole bodies (SPBs), organelles that serve as the centrosome in yeast cells and remain embedded in the nuclear envelope throughout mitosis⁹⁻¹¹. The γ TuC nucleates both spindle (nuclear) and astral (cytoplasmic) MTs¹²⁻¹⁴ and γ -tubulin bound to SPBs has been proposed to be in the form of “active” (nucleation competent) γ TuCs¹⁵. The pool of γ -tubulin bound to purified SPBs is phosphorylated at eight residues: two (T130 and T227) are specific to cells arrested in G1 and six (S42, S43/T44, S360, Y362, S444 and Y445) are specific to cells arrested in metaphase¹⁶. Residues S360, Y362 and Y445 (Fig. 1a) are evolutionarily conserved^{16,17}. Phosphorylation of residues S360, Y362 and Y445 occurs during metaphase and before the anaphase transition¹⁶, a time in the cell cycle that is functionally relevant to spindle assembly and sister chromatid attachment¹⁸.

The conservation of S360, Y362 and Y445 between yeast and human¹⁶ suggests phospho-regulation of these residues is a general mechanism for controlling the activity of γ -tubulin. To date, there is no evidence that phosphorylation of the pool of γ -tubulin bound to the SPBs contributes to the activation of γ TuCs¹⁵. Phosphorylation of S360 and Y445 likely contributes to events in spindle assembly (Fig. 1b). Mutation of S360 alters the number of anti-parallel MTs that provide stability to the spindle; an alanine substitution at this residue increases the number of anti-parallel MTs and stabilizes the spindle, while substitutions such as aspartic or glutamic acid that introduce a local negative charge and mimic constitutive phosphorylation, block the formation of anti-parallel MTs and decreases spindle stability¹⁹. Mutation of Y445 disrupts spindle function¹⁷ and causes chromosome loss²⁰; as a result, Y445D cells cannot survive in the absence of the spindle assembly checkpoint (SAC)^{17,21,22}. An internal deletion of S444, Y445 and their adjacent residues (DSYL) within the intrinsically disordered C-terminus

Department of Biology, McGill University, 3649 Promenade Sir William Osler, Montreal, Quebec, H3G 0B1, Canada. Kristian Shulist and Eric Yen contributed equally to this work. Correspondence and requests for materials should be addressed to J.V. (email: jackie.vogel@mcgill.ca)

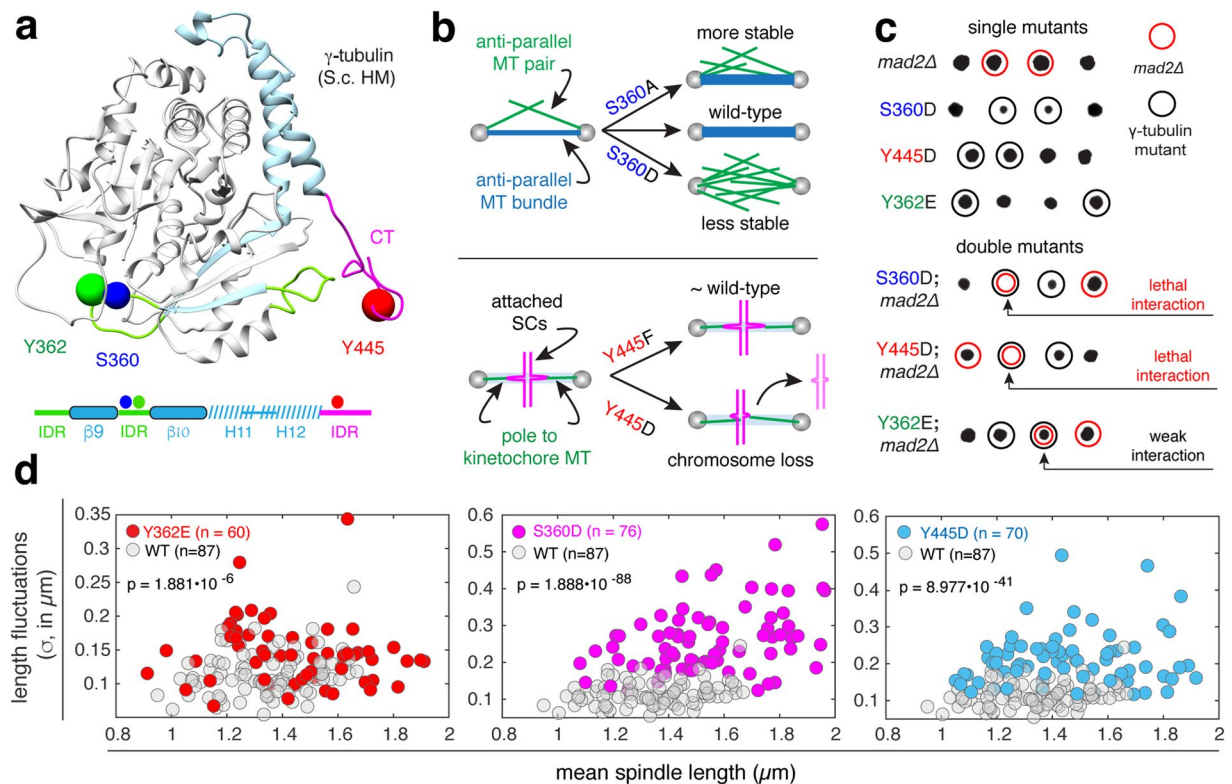


Figure 1. Effects of γ -tubulin phosphomimetic (D/E) mutations on spindle function and spindle stability. **(a)** ribbon structure of yeast γ -tubulin (homology model based on the human γ -tubulin structure) with loops and structured domains in the final 132 residues shown in green and blue, the predicted intrinsically disordered (ID) c-terminus is shown in pink. Spheres (0.25 nm) indicate the positions of the side chains of residues known to be phosphorylated at SPBs *in vivo*; S360 (blue), Y362 (green) and Y445 (red). A schematic representing the primary sequence of the 132 residues is shown below with ID regions shown in green, the α -helices and β -strands shown in dashed blue and solid blue (respectively), and the C-terminus shown in pink. **(b)** Cartoon depicting the role of S360 in architecture of the anti-parallel microtubule (MT) bundle and spindle stability (left panel); schematic depicting the role of Y445 in the attachment of sister chromatids (SCs) and resulting chromosome loss (right panel). **(c)** Tetrad dissections of γ tub-S360D, γ tub-Y445D and γ tub-Y362E, alone and in combination with *mad2* Δ . Unlike γ tub-S360D and γ tub-Y445D, the γ tub-Y362E *mad2* Δ double mutant is viable, with a slight growth defect, at 25°C. **(d)** Spindle length fluctuations in wild-type, γ tub-Y362E, γ tub-S360D and γ tub-Y445D cells, plotted as a function of mean spindle length. Fluctuations for each spindle (σ) are computed as the standard deviation of length.

perturbs both spindle assembly and pre-anaphase spindle positioning^{23,24}. As with S360 and Y445, Y362 is also evolutionarily conserved, however the biological function of this modification is unknown.

Separation-of-function mutations are extremely useful genetic tools in cell biology, and aid in understanding the biological significance of γ -tubulin phospho-regulation. Separation-of-function mutations can be identified through the analysis of synthetic genetic interactions (SGIs) discovered by conducting synthetic genetic array (SGA) screens²⁵. The SGA screen is a robotic-assisted method used to assess genetic interactions of mutations arrayed on plates; typically the array consists of non-essential gene knock-outs^{26–29}. The relative growth of each strain (wild-type controls, query, array and double mutants) is extracted using end-point analysis of colony size, with the growth of the double mutant compared to that of each single mutant; if the double mutant has an unexpected phenotype, an SGI is inferred. For null or loss-of-function mutations, the SGI profiles of functionally redundant genes converge, with genes in one pathway showing strong congruence in interactions with those in parallel, redundant pathways²⁹. However, a subset of unique SGIs is expected in the case of separation-of-function mutations when comparing SGI profiles for a series of alleles. Analysis of alleles presents an additional challenge, as they may exhibit phenotypic differences dependent on the process that is perturbed by the mutation. For example, an allele with a mutation that perturbs one of two spindle positioning pathways may exhibit a weak phenotype in comparison to an allele with a mutation that perturbs chromosome attachment. An SGA-based approach for detection of separation-of-function mutations must therefore be sensitive to differences in relative fitness of both single and double mutants, and also be precise in measurements such that SGI profiles for multiple alleles of the same gene can be compared.

In this study, we describe GAMER (Genetic Array with Mixed Effects Regression), a time-resolved and fitness-based SGA method, and used this approach to perform a comparative functional analysis by extracting

SGIs of two γ -tubulin alleles (γ tub-Y362E and γ tub-Y445D) used as query mutations in combination with ~4,700 SGA deletion mutations. Growth rates were computed and used to calculate the fitness of wild-type controls, and query, array and double mutants, and to compare relative fitness of mutants across the two γ -tubulin query alleles. The SGI profile for the previously described γ tub-Y445D mutation¹⁷ was enriched for genes that are involved in spindle assembly and stability, act in chromosome segregation, or function in the SAC, monitoring the fidelity of sister chromatid attachment. The SGI profile for the γ tub-Y362E mutation showed convergence with the γ tub-Y445D mutant for a subset of genes involved in mitosis, but also had a distinct set of SGIs with genes acting in spindle positioning and alignment relative to the future plane of cell division, as well as cell polarity. Live cell analysis of spindle stability and movements relative to the bud neck and polarity axis revealed that the γ tub-Y362E mutation does not alter spindle stability but is defective in pre-anaphase spindle alignment. We report that in the γ tub-Y362E mutants, the number of astral MTs is increased, and the bias of astral MTs to the old SPB relative to the new SPB is lost, leading to inefficient spindle alignment. Our results provide new evidence that the phosphorylation of an evolutionarily conserved tyrosine residue (Y362) contributes to γ -tubulin function in controlling the number of astral MTs associated with both SPBs of the metaphase spindle, and influences the efficiency of pre-anaphase spindle alignment relative to the future plane of cytokinesis.

Results

The γ tub-Y362E mutation does not reduce spindle stability. Cells with defects in spindle function require the activity of the SAC for survival, and typically die in the absence of checkpoint proteins²². The viability of tub4 alleles and their dependence on SAC activity was tested by analysis of progeny (tetrads; 20 per strain) obtained from diploids heterozygous for γ -tubulin alleles γ tub-S360D, γ tub-Y445D or γ tub-Y362E and the *mad2* Δ null mutation which blocks SAC activation. γ -Tubulin mutations S360D, Y445D and Y362E are viable under normal growth conditions (25–30 °C), with a weak growth defect observed for γ tub-S360D and γ tub-Y445D^{16,17} and Fig. 1c). As previously shown, the γ tub-S360D and γ tub-Y445D mutations are lethal in combination with the *mad2* Δ mutation^{16,17} while the Y362E mutant did not show similar sensitivity to the loss of the SAC (Fig. 1d).

We next examined fluctuations in spindle length, which reports relative spindle stability¹⁹. Length fluctuations were computed from the standard deviation of spindle length (σ) and assessed with respect to the mean spindle length (Fig. 1e). The γ tub-S360D mutation disrupts the formation of inter-polar anti-parallel cross-linked MTs¹⁹, and spindles in γ tub-S360D cells are unstable and undergo very large length fluctuations relative to wild-type cells ($p = 1.888 \times 10^{-85}$). In γ tub-Y445D cells, spindles experience large length fluctuations relative to wild-type cells ($p = 8.977 \times 10^{-41}$). The length fluctuations of spindles in γ tub-Y362E cells are similar to those of wild-type spindles ($p = 1.881 \times 10^{-6}$), and both wild-type and γ tub-Y362E spindles are stable relative to the spindles of γ tub-S360D and γ tub-Y445D mutants.

GAMER analysis reveals common and distinct SGIs of γ tub-Y362E and γ tub-Y445D alleles.

GAMER analysis uses a modified SGA method that provides a growth rate parameter. After the final pinning for selection of *MATa* double mutants, plates were imaged at two hour intervals for 72 hours (movie M1). Colony size and density were extracted from the resulting images and used to calculate growth rate and relative fitness of each strain (Fig. 2a). Linkage group analysis for the *TUB4* locus extending 150 kilobases in both directions (approximately 50 centiMorgans^{30–32}) was conducted using both GAMER and a standard growth characterization method (Supplemental Figure S1). Due to technical issues arising from experimental procedures (i.e. colony position on the array plate), growth characterization of the endpoint colony sizes had much larger variances. These issues can be corrected during post-processing³³. In contrast, the resulting GAMER growth rates for the *TUB4* linkage groups had a higher measured precision and showed more uniformity across the genes without additional post-processing.

In agreement with the *mad2* Δ genetic analysis shown in Fig. 1c, γ tub-Y445D was found to have a strong synthetically lethal interaction with *mad2* Δ (relative fitness of 0%, $p < 10^{-4}$, Fig. 2b). GAMER is also suitable for detection of weak SGIs; the γ tub-Y362E mutation had a weak but significant interaction with *mad2* Δ (relative fitness of 61%, $p = 8.88 \times 10^{-3}$, Fig. 2c) revealing an interaction that was not apparent when colony sizes of γ tub-Y362E and *mad2* Δ were compared with the double mutant (Fig. 1c). Fitness-based experiments using GAMER overcome potential technical variations that could influence the interpretation of results; for example *mad2* Δ colonies appear to increase in size faster than wild-type due to their increased endpoint densities (Fig. 2b,c; left panels), however, our analysis reveals that the growth rates of *mad2* Δ and wild-type colonies are not statistically different (Fig. 3B,C).

GAMER identified 1035 SGIs across the γ tub-Y362E and γ tub-Y445D screens (Fig. 3a and supplemental dataset 1). To directly compare the relative fitness between SGIs of the two alleles, we projected the two sets of GAMER scores (γ tub-Y362E and γ tub-Y445D) for each array mutant. This organized SGIs into groups: rescues, where the fitness of the γ -tubulin allele (Y445D) was increased as a result of the array mutant, or the fitness of the array mutant increased when combined with the γ tub-Y362E or γ tub-Y445D allele, or synthetic sick or lethal SGIs where the fitness of the γ -tubulin allele combined with the array mutant was reduced. Genes in the linkage group (Fig. 3c, pink) tend to cluster close to the boundary (—) between where one γ -tubulin allele is reduced more than the other (i.e. where fitness is equivalently reduced for both γ tub-Y362E and γ tub-Y445D).

Comparison of the GAMER-derived SGIs of γ tub-Y362E and γ tub-Y445D mutants revealed that the proportion of SGIs common to both alleles was smaller than the set of SGIs unique to each allele. We identified 123 SGIs in common for γ tub-Y445D and γ tub-Y362E, and a larger number of unique SGIs, with 524 SGIs for γ tub-Y445D and 380 SGIs for γ tub-Y362E. γ Tub-Y362E did not have an SGI with the *mad3* Δ mutation and the normalized scores for the γ tub-Y362E interactions with *mad1* Δ and *mad2* Δ mutations were less severe than the corresponding scores for γ tub-Y445D (Fig. 3c and supplemental datasets). The γ tub-Y362E mutation had no

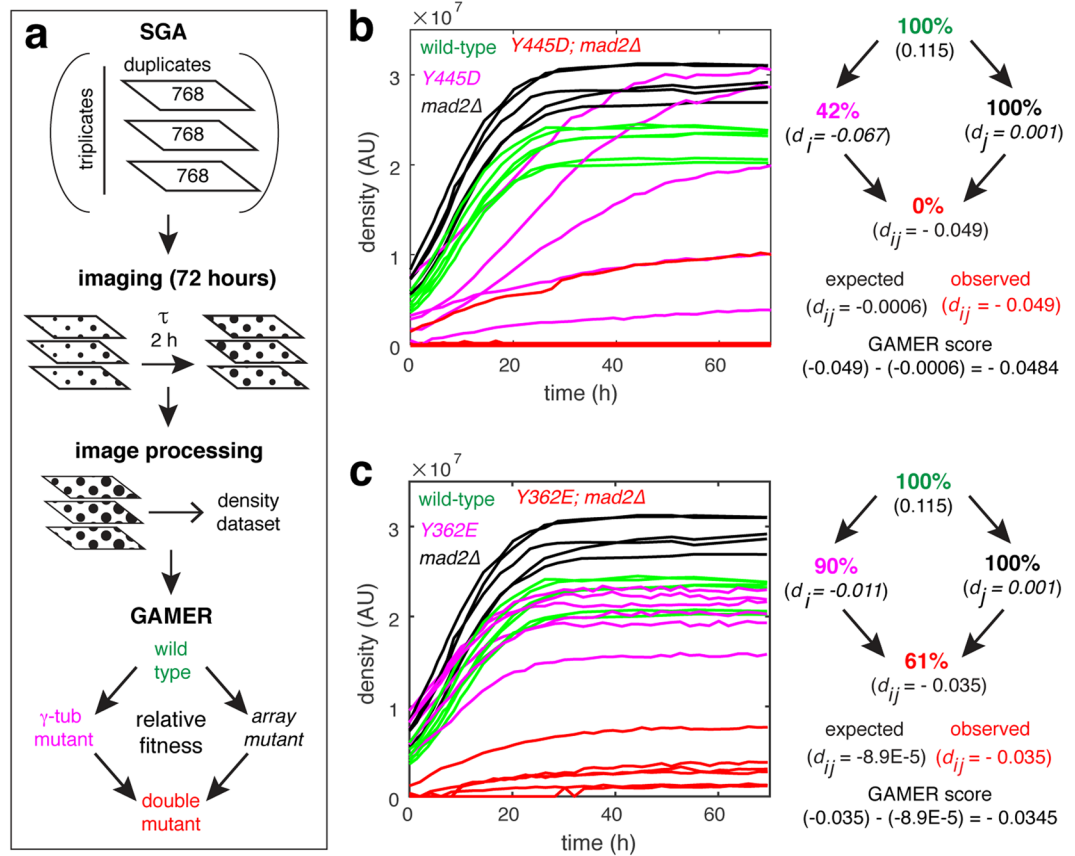


Figure 2. Identification of synthetic genetic interactions based on relative fitness using GAMER. (a) Overview of the GAMER method, which includes imaging every two hours over a 72-hour period. Images are processed computationally and fitness extracted and used to calculate the GAMER scores of the double mutants. (b,c) SGA growth curves (left panels) for six isolates of wild-type, γ tub-Y445D (top) or γ tub-Y362E (bottom), *mad2* Δ and the combined double mutant. Values of the observed and expected growth defects (d_{ij}) for the respective double mutants (right panels).

SGIs with mutations in genes that strictly contribute to the function of spindle/nuclear microtubules (Fig. 3d). In contrast, SGIs specific for the γ tub-Y445D allele were consistent with defects in both anti-parallel (*ase1* Δ and *slk19* Δ) and parallel (*vik1* Δ) nuclear MT cross-linking, the former is required to form the interpolar MTs that stabilizes the spindle^{34–37}. SGIs common to both alleles were often genes that function in both spindle MT and astral MT-dependent processes or coordinate the completion of spindle positioning/alignment with mitotic exit. *Cik1* Δ , which has been shown to function on both the spindle and astral MTs³⁸, was a common SGI for both alleles. The γ tub-Y362E SGI profile revealed a dependence on the cell cycle kinase *Kin4* (Fig. 3e), which inhibits the mitotic exit network (MEN) when the spindle positioning checkpoint is activated^{39,40}. Additionally, γ tub-Y362E SGI profile was enriched for SGIs with genes acting in *Kar9* and dynein-dependent spindle positioning and cell polarity (Fig. 3f). This group of SGIs included mutations in *bub2* Δ and *lte1* Δ , as well as mutations in components of the dynactin complex (*arp1* Δ , *jnm1* Δ , *ldb18* Δ , *nip100* Δ) and the kinase *Pac1*, both of which regulate the activity of cytoplasmic dynein during spindle positioning. SGIs specific to γ tub-Y362E also included components of the polarisome (*rho2* Δ , *bem3* Δ , *rom2* Δ , *rgl1* Δ) and actin cables (*abp140* Δ) that are critical for both *Kar9* and dynein dependent spindle positioning. These results suggested that the γ tub-Y362E mutation likely perturbs a function of γ -tubulin that is directly linked to spindle positioning and actin organization rather than the previously characterized role in spindle assembly (γ tub-S360D, γ tub-Y445D).

Despite their spatial separation in both the primary and tertiary structures of γ -tubulin, the γ tub-S360D and γ tub-Y445D mutants both exhibit spindle instability (Fig. 1a). Residues S360 and Y362 are positioned within an unstructured loop, close to each other in the primary and tertiary structure of γ -tubulin and on the opposite surface of the molecule to the intrinsically disordered C-terminal containing Y445. We asked if S360 and Y362 are functionally coupled with Y445 by assessing the viability of intra-molecular double mutants in S360 and Y445 as well as in Y362 and Y445. Individual phospho-inhibiting mutations (A or F) in S360, Y362 and Y445 were viable (Supplemental Figure S2a). Interestingly, intra-molecular double mutations S360A-Y445D or S360D-Y445F were lethal (Supplemental Figure S2b). Previously we reported that S360 phosphorylation by *Cdk1* requires the early mitotic cyclin *Clb3* *in vivo*⁴¹, and this may be the cause of the lethal interaction between the γ tub-Y445D and *clb3* Δ mutants (Fig. 3e). When mutations in Y362 and Y445 were combined, only the Y362F-Y445D double mutant showed a growth phenotype (Supplemental Figure S2c). Taken together with the GAMER results, our

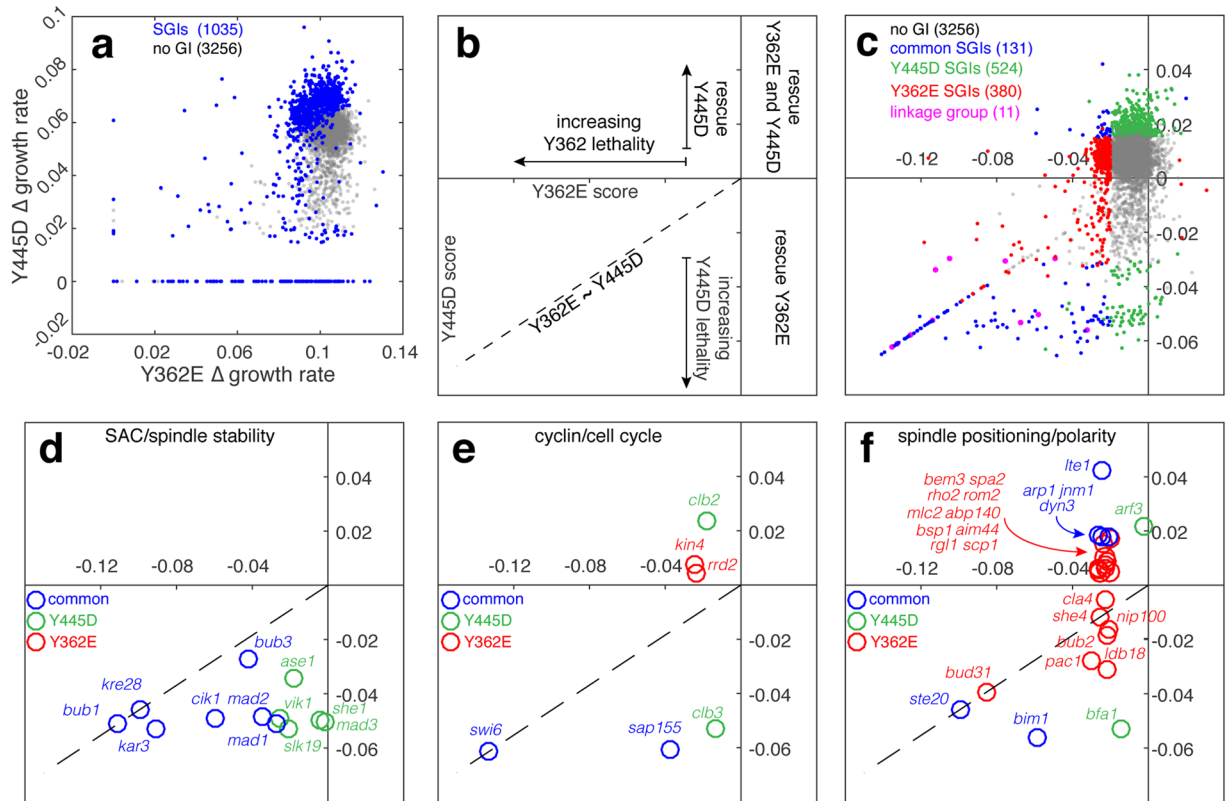


Figure 3. GAMER identifies distinct and common SGIs for γ tub-Y445D and γ tub-Y362E alleles. **(a)** Growth rates for all array mutants when combined with γ tub-Y445D were plotted against their growth rates when combined with γ tub-Y362E. The blue points represent all significant hits between the two GAMERS; grey represents the genes with no genetic interactions. Genes that caused lethal phenotypes when combined with γ tub-Y445D or γ tub-Y362E cluster along the x- or y-axis, respectively. **(b)** The resulting GAMER scores for γ tub-Y445D and γ tub-Y362E were projected onto the same axis organizing SGIs into four quadrants depending on the respective scores: [i] hits that reduced the relative fitness in both alleles (lower, left), [ii] hits that reduced fitness for γ tub-Y362E, but increased fitness (rescued) for γ tub-Y445D (upper, left), [iii] hits that increased fitness for γ tub-Y362E but reduced fitness for γ tub-Y445D (lower, right), and [iv] hits that increased fitness for both alleles (upper, right). Quadrant [i] is divided in half along a diagonal line (—) which indicates hits that reduced fitness similarly for both alleles. Above this line, fitness was reduced more for γ tub-Y362E than γ tub-Y445D while below this line, the opposite is true. **(c)** GAMER scores for all SGA mutants including those that were unique hits for γ tub-Y445D (green), those that were unique hits for γ tub-Y362E (red), those that were common hits for both alleles (blue), the linkage group (pink) and those that did not have SGIs with either allele (grey). **(d–f)** SGIs related to the SAC and spindle stability **(d)**, to the cell cycle **(e)**, and to spindle positioning and cell polarity **(f)**.

analysis of intramolecular genetic interactions suggests that phosphorylation of S360 and Y445 must be coordinated with respect to each other during spindle assembly, while phosphorylation of Y362 is uncoupled and regulates γ -tubulin activity in a process that involves genes acting in spindle alignment and cell polarity (Supplemental Figure S2d).

A geometric definition for perfect alignment of the metaphase spindle in budding yeast. A budding yeast cell is asymmetric once the bud has formed, with a polarity axis that is normal to the plane of the bud neck (the future site of cytokinesis). As the spindle is assembled, it becomes positioned close to the bud neck and is aligned parallel to the polarity axis and normal to the bud neck plane, with a strong bias for the older SPB (formed in the previous cell cycle) to be proximal to the neck⁴². This condition, which we define as perfect alignment, is the reference for our measurement of spindle alignment in wild-type and mutant cells (Fig. 4a). Perfect alignment ensures that the anaphase spindle will elongate through the bud neck and a full complement of chromosomes are inherited by the mother and daughter cells at the end of cell division. If the spindle is not positioned at the neck and/or not aligned normal to the bud neck plane, anaphase may occur in the mother cell, resulting in aneuploidy and cell death. To compare a spindle to this reference, we project it (in 3D) to a perfectly aligned spindle (1D). If the spindle is perfectly aligned, the true (3D) and projected (1D) lengths are approximately the same, while spindles rotated 90° off the polarity axis would have a projected length of 0. As spindle alignment proceeds, the true and projected length of the spindle are expected to converge.

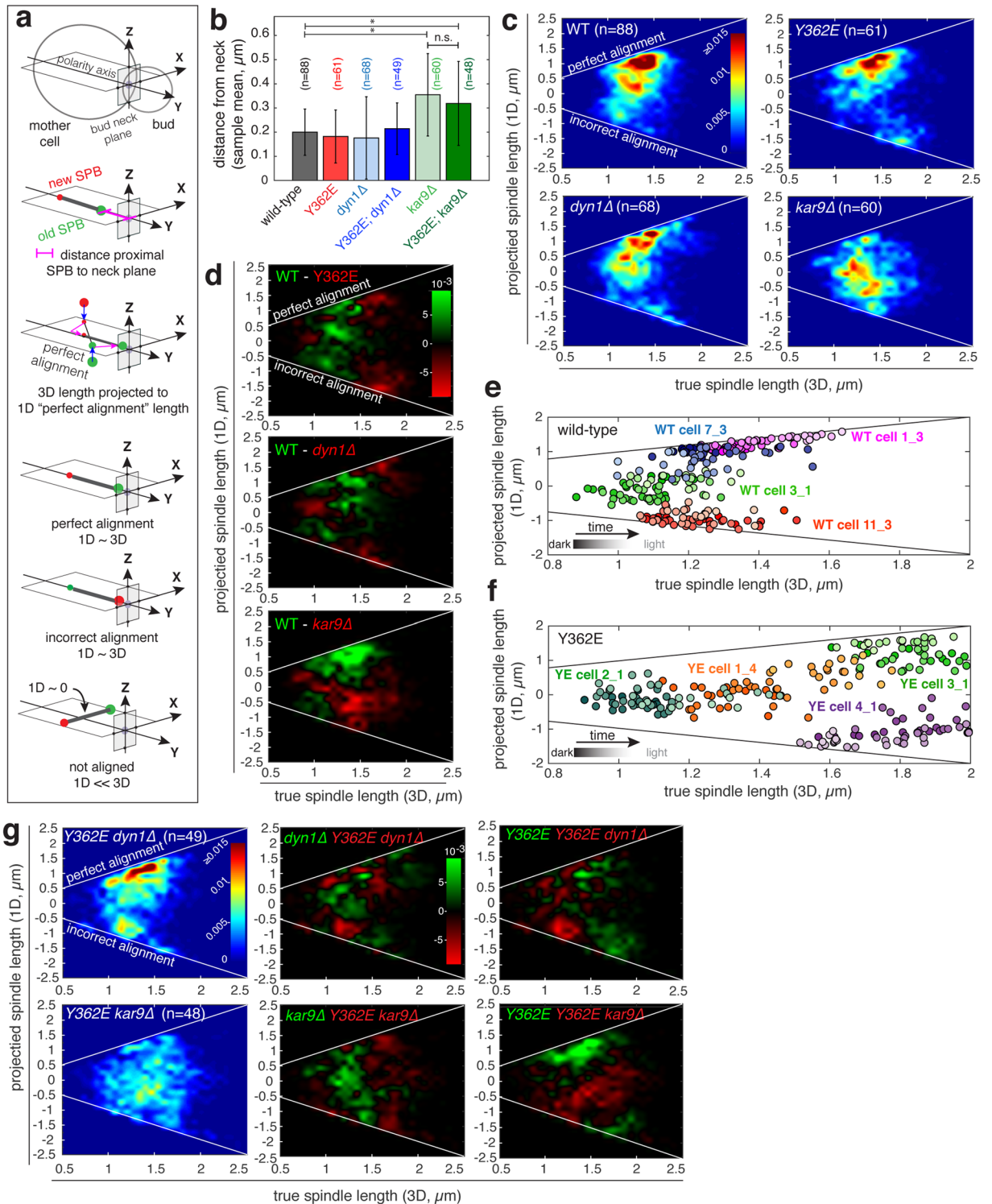


Figure 4. Pre-anaphase spindle alignment is perturbed in $\gamma\text{tub-Y362E}$ cells. **(a)** Schematic depicting the method used to compute the distance between proximal pole and bud neck (spindle positioning) and spindle alignment in relation to “perfect alignment”. Perfect alignment is defined as a spindle with a 1D projected spindle length $\sim 3\text{D}$ spindle length. **(b)** Distance of the proximal pole from the bud neck; error bars show standard deviation. *Indicates statistical difference with $p < 0.0001$; n.s. denotes no significant difference. **(c)** Heatmaps showing the projected 1D spindle length as a function of true 3D spindle length in wild-type (WT), $\gamma\text{tub-Y362E}$, $\text{dyn1}\Delta$ and $\text{kar9}\Delta$ cells. Color bar shows the frequency of time points normalized to the total number of time points of all cells. Incorrect alignment occurs when the new pole is proximal to the bud. **(d)** Difference map comparing WT (shown in c; upper left) to $\gamma\text{tub-Y362E}$ (top), $\text{dyn1}\Delta$ (middle) and $\text{kar9}\Delta$ (bottom). Green indicates areas where the frequency of the WT was increased relative to the mutant, red indicates areas where the frequency of the mutant was increased relative to WT. Instantaneous projected 1D spindle length plotted as a function of true 3D spindle length of representative **(e)** WT and **(f)** $\gamma\text{tub-Y362E}$ cells.

Time is indicated by the color gradation from dark (start) to light (end). (g) The γ tub-Y362E mutation increases the range of unaligned spindle orientations and incorrect alignment when combined with *kar9 Δ and *dyn1* Δ mutants. Heatmaps showing the projected 1D spindle length in double mutants γ tub-Y362E; *dyn1* Δ (upper left) and γ tub-Y362E; *kar9* Δ cells (lower left). Plots showing the differences between the single mutants and double mutants. Green indicates areas where the frequencies of the single mutant were larger than the double mutants, red indicates areas where the frequencies of the double mutant were increased.*

The γ tub-Y362E mutation does not perturb spindle positioning at the bud neck. We measured spindle positioning at the bud neck in wild-type and γ tub-Y362E cells, as well as in mutants lacking either cytoplasmic dynein (*dyn1* Δ) or the APC-like + tip protein, Kar9 (*kar9* Δ), both of which are central to the two functionally redundant spindle positioning pathways in budding yeast. To measure spindle position relative to the bud neck, we analyzed the trajectory of the SPBs, which are diffraction limited point-like objects whose position can be precisely determined^{19,43}, over a ten-minute window in single cells and extracted the mean distance of the proximal SPB to the neck plane and the mean spindle length using 3-dimensional data collected at ten second intervals. The distance of the proximal SPB to the neck plane was computed for metaphase spindles with an average length $<2\ \mu\text{m}$ and initial lengths between $0.8\ \mu\text{m}$ and $2\ \mu\text{m}$ for wild-type ($n = 88$ cells), single mutant (γ tub-Y362E $n = 61$ cells; *kar9* Δ $n = 60$ cells; *dyn1* Δ $n = 68$ cells) and double mutant strains (γ tub-Y362E *kar9* Δ $n = 48$ cells; γ tub-Y362E *dyn1* Δ $n = 49$ cells). In the majority of wild-type, γ tub-Y362E, *dyn1* Δ and γ tub-Y362E *dyn1* Δ cells, the normalized mean distance of the proximal pole to the neck is less than 25% of the diameter of the mother cell regardless of the mean length of the spindle (Fig. 4b and Supplemental Figure S3). In contrast, in the majority of *kar9* Δ and γ tub-Y362E *kar9* Δ cells, the mean distance of the proximal pole to the neck is $>25\%$ of the diameter of the mother cell and is significantly increased relative to wild-type, as well as to the other mutants ($p < 0.0001$; Fig. 4b and Supplemental Figure S3). Movement of the spindle to the neck occurs even in the absence of cytoplasmic dynein, and is not significantly perturbed by the γ tub-Y362E mutation.

Spindle alignment is defective in the γ tub-Y362E mutant. For each strain (wild-type or mutant), alignment is shown as the normalized frequency of projected (1D) lengths in a distribution of 3D length bins for all time points; two white lines indicates where 1D and 3D length converge, either perfect alignment (aligned, old SPB proximal to neck) or incorrect alignment (aligned, new SPB proximal to neck). In wild-type cells, perfect alignment is correlated with increasing 3-dimensional spindle length, with most spindles $\geq 1.5\ \mu\text{m}$ in length maintaining perfect alignment (Fig. 4c, upper left panel). In the γ tub-Y362E mutant, spindles exhibit a defect in achieving or maintaining perfect alignment, and the frequency of incorrect alignment of spindles $>1.5\ \mu\text{m}$ in length is increased relative to wild-type (Fig. 4c, upper right panel). Spindle alignment is observed in *dyn1* Δ cells (Fig. 4c, lower left panel), however the majority of spindles in *kar9* Δ cells do not achieve or maintain perfect alignment regardless of spindle length (Fig. 4c lower right panel). Instead, spindles in *kar9* Δ cells tend to explore orientations centered around a parallel alignment to the bud neck and 90° to the polarity axis (i.e. projected 1D length of zero). We directly compared spindle alignment in wild-type cells with mutants by computing the difference between the conditions, with wild-type compared to γ tub-Y362E, *dyn1* Δ or *kar9* Δ (Fig. 4d). Spindles in γ tub-Y362E cells explore many orientations relative to the bud neck plane. The frequency of incorrect alignment is increased in both γ tub-Y362E cells, and to a lesser amount in *dyn1* Δ cells, relative to wild-type cells.

To better understand the nature of the defect in spindle alignment in γ tub-Y362E cells, we plotted instantaneous projected spindle length as a function of true spindle length for representative wild-type and γ tub-Y362E cells taken from mean 3D length bins of $1\ \mu\text{m}$, $1.3\ \mu\text{m}$ and $1.5\ \mu\text{m}$ (Fig. 4e,f). In wild-type cells, spindles with an average length less than $1.2\ \mu\text{m}$ are not aligned, however longer spindles either undergo alignment or remain aligned during the ten minutes of observation (Fig. 4e and supplemental movies M2–M5). In contrast, in γ tub-Y362E cells, spindles are frequently misaligned independent of spindle length, and approach but do not maintain perfect alignment as spindle length increases (Fig. 4f, and supplemental movies M6–M9).

The γ tub-Y362E mutation enhances alignment defects of Kar9 and dynein mutants. To understand how the γ tub-Y362E mutation might affect the function of Kar9 or dynein, we next investigated spindle alignment in γ tub-Y362E cells in combination with *dyn1* Δ or *kar9* Δ mutations. When γ tub-Y362E is combined with *dyn1* Δ , such that spindle alignment is dependent on Kar9, the frequency of incorrect alignment increases for spindles $\leq 1.5\ \mu\text{m}$ (Fig. 4g, upper panels). Interestingly, while the majority of spindles in *kar9* Δ cells were biased to orientations parallel to the bud neck axis (i.e. projected 1D length of zero; Fig. 4c), in γ tub-Y362E *kar9* Δ double mutants, spindle orientation appears to be random relative to the bud neck plane (Fig. 4g, lower panels).

The Y362E mutation increases the number of astral MTs at the old and new SPBs. Forces produced by astral MTs are important for spindle positioning and alignment^{44–47}. Thus, we investigated the effect of the γ tub-Y362E mutation on the behavior and number of astral MTs in metaphase cells. Representative wild-type and γ tub-Y362E cells expressing a Venus-Tub1 (α -tubulin) MT reporter and a Spc42-Cerulean SPB reporter are shown in Fig. 5a and supplemental movies M10–M15. In wild-type cells, pre-anaphase spindles typically have one to two astral MTs (mean of 1.28 ± 0.568), in agreement with published data⁴⁸. Pre-anaphase spindles in the γ tub-Y362E mutant had almost two-fold more astral MTs than wild-type (mean of 2.59 ± 0.616 , $p = 1.5 \times 10^{-9}$).

We next investigated the astral MT number at each SPB. Astral MTs associated with the pre-existing (old) SPB are thought to persist longer due to an increased stability cause by the asymmetric loading of MT + tip proteins, such as Bim1 and Kar9, during spindle alignment^{49–51}. The increased stability of astral MTs loaded with + tip proteins likely contributes to the increased number of astral MTs associated with the old SPB (0.89 ± 0.312) relative

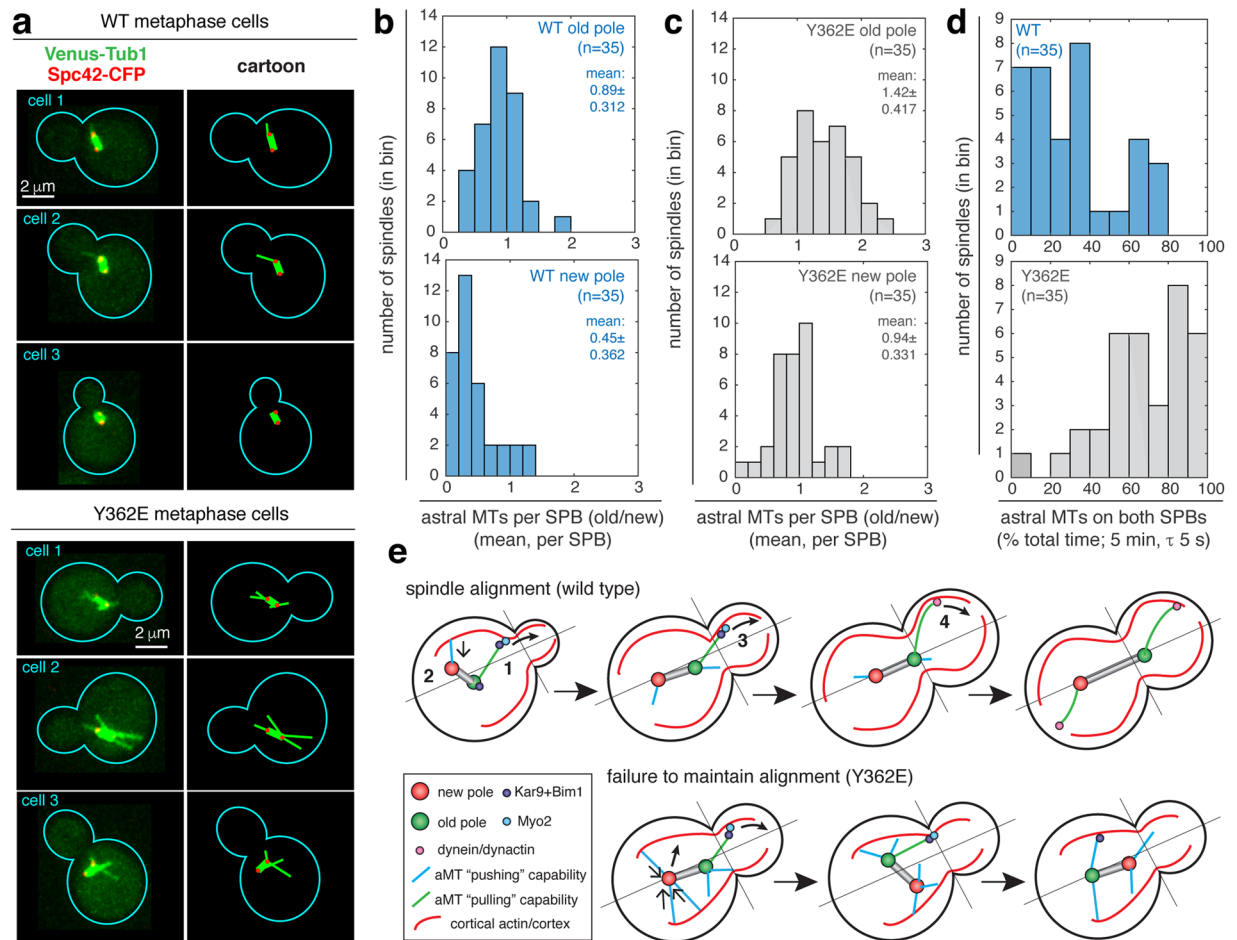


Figure 5. The number of astral MTs associated with old and new SPBs is increased in γ tub-Y362E cells. **(a)** Representative metaphase spindles (two SPBs 0.8 to 2 μm apart) in wild-type (WT) and γ tub-Y362E cells. MTs are tagged with Venus-Tub1 (shown in green) and SPBs tagged with Spc42-Cerulean (shown in red). Corresponding explanatory schematics for astral MT organization are shown to the right. **(b,c)** Astral MT count for old and new SPBs in wild-type **(b)** and γ tub-Y362E **(c)** cells. **(d)** Percentage of total time both SPBs have astral MTs in WT and γ tub-Y362E cells. **(e)** Proposed mechanism for loss of alignment in γ tub-Y362E cells. (1) During normal spindle alignment, Kar9-Bim1 complexes are loaded onto astral MTs and track the plus end. Kar9 binds to the type 5 myosin Myo2 which guides the astral MT plus end to the bud by walking on actin cables that originate at the bud cortex, while astral MTs projecting into the mother cell, regardless of their association with Kar9-Bim complexes, are short lived. (2 and 4) Astral MTs terminating in the bud exert a “pulling” force, via Kar9 or dynein, (3) astral MTs terminating in the mother are capable of “pushing” the spindle away from the mother cell cortex. An increase in the number of astral MTs in γ tub-Y362E cells results in uncoordinated pushing and pulling forces (via Kar9 or dynein) at both SPBs, resulting in failure to achieve or maintain spindle alignment.

to the new SPB (0.45 ± 0.362 , $p = 1.1 \times 10^{-6}$) in wild-type cells (Fig. 5b). However, in γ tub-Y362E cells, the number of astral MTs is increased on both old and new SPBs relative to wild-type (Fig. 5c). The number of astral MTs associated with the old SPB increased 1.6-fold (1.42 ± 0.417 , $p = 1.1 \times 10^{-6}$) and the number of astral MTs associated with the new SPB increased 2-fold (0.94 ± 0.331 , $p = 1.0 \times 10^{-6}$). Interestingly, despite having increased numbers of astral MTs, only one astral MT entered the bud at a time in Y362E cells, as is seen in wild-type (Supplemental Figure S4). The increase in the number of astral MTs at both old and new SPBs in γ tub-Y362E cells results in a significant shift towards symmetry of astral MT occupancy, defined as having at least one astral MT on both SPBs over the five-minute acquisition window (e.g. 80% symmetry of astral MT occupancy indicates the cell has at least one astral MT on both poles for 80% of the acquisition time), and away from the bias of astral MT occupancy asymmetry to the old SPB found in wild-type cells (Fig. 5d, $p = 1.3 \times 10^{-7}$). In the γ tub-Y362E mutant, 40% of cells (14 of 35 cells) had $\geq 80\%$ symmetry of astral MT occupancy, a condition that was not observed in wild-type cells ($n = 35$). Over 80% of γ tub-Y362E cells (29 cells) had astral MTs on both SPBs during at least 50% of the five-minute acquisition window, while in wild-type cells, the frequency of symmetry of astral MT occupancy $\geq 50\%$ was relatively rare (8 cells, 23%). Our analysis suggests that the majority of movements of the spindle during pre-anaphase spindle positioning in γ tub-Y362E cells are predominantly influenced by astral MTs associated with both old and new SPBs, rather than by astral MTs associated with the old SPB as in wild-type cells.

Discussion

In this study, we developed GAMER, a novel SGA-based approach that identifies subtle differences amongst alleles of one gene (γ tub-Y445D, γ tub-Y362E). In previous SGA screens, the assumption that SGIs are rare events⁵² forms the basis of the analysis, leading rare to be defined contextually amongst the queried double mutants. In contrast, GAMER measures growth rates of individual colonies in combination with mixed effects regression to overcome the limitations that are solved by assuming SGIs are rare, leading to an increased sensitivity in the method. It is ideally suited for discerning the subtle differences between an allelic series and also for identifying SGIs of mutants with subtle growth phenotypes such as the γ tub-Y362E mutant. The sensitivity and precision of the GAMER approach enabled the detection of a set of specific SGIs for the γ tub-Y362E allele that revealed sensitivity to mutations in genes acting in spindle positioning/alignment and cell polarity, but not to mutations in genes acting in spindle assembly or the spindle assembly checkpoint. These results motivated a quantitative analysis of spindle positioning and alignment; this led to the first instance of evidence that phosphorylation of Y362 may control the number of astral MTs during spindle positioning. Lastly, our method can uniquely be applied to both large-scale and small-scale assays, allowing the functional screening of new candidates using sub-arrays of the SGA. Taken together, and considering its success in detecting subtle differences between γ -tubulin alleles, we believe GAMER to be a useful improvement on the standard SGA method as it facilitates the comparative analysis of an allelic series and aids in the identification of separation-of-function mutants.

GAMER results indicated that the γ tub-Y445D and γ tub-Y362E alleles perturb different aspects of γ -tubulin's function, with the former acting in spindle assembly as previously described¹⁷, and the latter involved in spindle alignment relative to the bud neck plane. Our high-throughput GAMER results recapitulate previous SGIs identified by tetrad dissection^{17,24} and the identified γ tub4-Y445D SGIs are consistent with a previously reported decrease in chromosome transmission fidelity in this mutant²⁰. We confirmed the latter result by quantitatively measuring the ability of a metaphase spindle to reach the state of perfect alignment in wild-type, the γ tub-Y362E mutant, and spindle positioning and alignment mutants *kar9* Δ and *dyn1* Δ . Unexpectedly, we found that γ tub-Y362E cells have an increased number of astral MTs on both old and new SPBs, which reduces the asymmetry of astral MT pole occupancy that is normally biased to the old SPB relative to the new SPB. The increase in astral MT symmetry is correlated with an increase in the frequency of spindle misalignment independent of spindle length.

GAMER analysis combined with analysis of intra-molecular mutations provided new insights into the role of S360 and Y445 phosphorylation in spindle assembly. Mutations that substitute negatively charged amino acids (D/E) at S360 and Y445 decrease spindle stability^{17,19} and this study). This instability is not due to a lack of spindle MTs, but instead arises from a defect in the organization of these MTs, in particular the formation of a stabilizing core bundle of anti-parallel inter-polar MTs, which is promoted in the γ tub-S360A mutant and defective in the γ tub-S360D mutant^{17,19}. The *ase1* Δ and *slk19* Δ SGIs with the γ tub-Y445D allele are consistent with a similar defect in the function of the inter-polar MTs of the spindle. The phosphorylation state of S360 and Y445 may be involved in tuning the architecture of the spindle MTs, with phosphorylation state either promoting MT cross-linking (S360 and/or Y445 unphosphorylated) or preventing excessive or inappropriate MT cross-linking (S360 and/or Y445 phosphorylated). Despite their similar phenotypic output of spindle instability, the lethality of the intra-molecular γ tub-S360A-Y445D mutant suggests that phosphorylation of S360 and Y445 are likely to be independent events during spindle assembly.

In budding yeast, there are two pathways that can execute pre-anaphase spindle positioning and alignment: the *Kar9/Bim1/Myo2* pathway (APC/EB1/Myosin V in metazoans) and the dynein pathway, both of which act by applying a pulling force on astral MTs and, as a result, on the spindle as well^{53–56}. We investigated both of these pathways' role in the achievement of perfect alignment (where the spindle must translocate towards the bud neck, and align with the old SPB proximal to the bud neck plane). The process of spindle translocation and alignment begins in early metaphase, and in the absence of *Kar9*, short spindles (<2 μ m in length) fail to achieve perfect alignment. We found that spindles in *kar9* Δ cells are frequently oriented parallel to the bud neck plane, consistent with previous studies demonstrating that the *kar9* Δ mutant exhibits defects in alignment as well as nuclear migration^{54,57}. Deletion of dynein did not affect spindle translocation to the bud neck plane, but resulted in an increase in time points where the new SPB is proximal to the bud neck (incorrect spindle alignment). Our results confirm that *Kar9* is the dominant pathway for early spindle positioning and alignment.

Our analysis of spindle alignment in the presence of the Y362E mutant combined with *dyn1* Δ or *kar9* Δ mutations reveals that both pathways depend on astral MT asymmetry to achieve perfect alignment (Fig. 4e). In the absence of *Kar9*, the γ tub-Y362E mutation enhances misalignment such that spindles appear to explore many more orientations; this observation suggests that dynein may be sensitive to the increase in astral MT number at both old and new SPBs, and/or symmetry of pole occupancy resulting from the γ tub-Y362E mutation. This would be unexpected, as the asymmetry of dynein to the astral MTs of the old SPB in late-metaphase has previously been shown to be independent of astral MT number and symmetry⁵⁸. The increase in astral MTs on both SPBs therefore may lead to an increase in pushing forces applied to both old and new SPB of the spindle that arise from the polymerization of astral MTs rather than *Kar9* or dynein. When the plus ends of astral MTs come into contact with the cortex of the mother cell, the MT exerts a pushing force on the SPB, causing it to displace⁵⁵; astral MT pushing forces are also observed in G1 cells, prior to SPB separation⁵¹. Pushing forces applied by astral MTs do not interfere with spindle positioning at the bud neck⁵⁹ if properly balanced by astral MTs that exert pulling force on the old SPB.

Kar9 and dynein can both pull astral MT plus ends into the bud through their association with cortical actin. Due to the asymmetric localization of *Kar9* and dynein, pulling forces are almost exclusively biased to the old SPB in wild-type cells. Pulling forces are usually restricted to one bud-directed astral MT at a time (supplemental Fig. S4); this is likely why *Kar9*-FP is typically only seen at one focus at a time^{44,49,54}. Every astral MT has the potential to apply either a pulling force (bud-directed) or a pushing force (mother-directed). If there is an increase

in the number of astral MTs at both SPBs (i.e. a shift towards astral MT occupancy symmetry), as is seen in the γ tub-Y362E mutant, an increase in the frequency of pushing forces by astral MT at both SPBs will compete with pulling forces that are biased to the astral MTs of one SPB (Fig. 5e). Interestingly, wild-type and γ tub-Y362E cells have at most a single bud-directed astral MT at any time (supplementary Fig. S4). This suggests that the surplus of astral MTs projecting into the mother cell in the γ tub-Y362E mutant are applying pushing forces. As a result, γ tub-Y362E cells must contend with the potential for pushing and pulling forces applied to the old pole. Taken together, these consequences are expected to produce spindle movements that are decoupled from the polarity axis of the cell that we observe in γ tub-Y362E cells.

γ -Tubulin phospho-regulation appears to contribute to both spindle assembly and alignment/positioning (17,19 and this study), processes that occur in the nucleus and cytoplasm, respectively. Given the unaltered spindle stability as well as ~2-fold increase in astral MTs, we speculate Y362 phosphorylation occurs in the cytoplasmic compartment of the cell. As well, we suggest that S360 and Y445 phosphorylation occurs in the nucleus and mainly affects those MTs and their organization. Phosphorylation may also be restricted to a sub-population of γ -TuRCs in both compartments. Kollman *et al.* proposed that S360 and Y362, which are located on the inner side of the γ -TuRC, can only be accessed by a kinase when the γ -TuRC is not occupied by a MT¹⁵. Phosphorylation of Y362 is therefore likely to occur prior to nucleation of a MT by the γ -TuRC.

The appearance of metaphase spindles in γ tub-Y362E cells is similar to metaphase spindles in wild-type cells (Fig. 5a and supplemental movies M10–M15) and it is unclear whether the number of spindle MTs is increased by the γ tub-Y362E mutation. The budding yeast kinetochore binds a single MT, and thus surplus spindle MTs would increase the number of anti-parallel cross-linked inter-polar MTs which has been shown to not significantly alter spindle function¹⁹. In wild-type cells, the formation of inter-polar MTs does not compete with the capture of kinetochores by free MT plus ends⁶⁰, and cross-linking proteins such as Ase1 or Cin8 may limit the number of stable inter-polar MTs that can be formed¹⁹. Spindle MTs not bound to a kinetochore or another MT are relatively unstable, and for this reason the formation of surplus spindle MTs during spindle assembly may not result in major changes in spindle architecture.

The Y362E mutation introduces a negatively charged amino acid (E) in place of a tyrosine known to be phosphorylated *in vivo*¹⁶, and suggests that phosphorylation of Y362 is likely to increase the number of astral MTs, either by stabilizing and thereby increasing the lifetime of astral MTs or by favoring the formation of astral MTs. Surprisingly, the increase in symmetry of astral MT occupancy we observed in γ tub-Y362E cells appears to not block translocation of the spindle to the bud neck in the absence of dynein, suggesting that Kar9 is functional even when astral MTs are present on both SPBs^{49,57,61}. Furthermore, while both old and new SPBs are associated with more astral MTs in the majority of spindles in γ tub-Y362E cells, the number of astral MTs associated with the old SPB (1.42 ± 0.412) is greater than that of the new SPB (0.94 ± 0.331 , $p = 8.2 \times 10^{-6}$); in fact, the difference in astral MT number between the old and new poles does not change significantly between wild type and γ tub-Y362E (0.44 ± 0.081 and 0.48 ± 0.090 , respectively; $p = 0.92$). This suggests that although astral MT occupancy becomes symmetric, factors contributing to differences in astral MT number remain active in γ tub-Y362E cells. Regardless of the mechanism by which the number of astral MTs is increased, our analysis of the γ tub-Y362E mutant suggests that γ -tubulin contributes to determining the number of astral MTs associated with the spindle during metaphase, and consequently contributes to spindle alignment. Our findings raise several fascinating questions for future studies. We speculate that phosphorylation of Y362E may increase the number of astral MTs associated with the old SPB, and increase the efficiency of pre-anaphase spindle alignment by Kar9. Alternatively, phosphorylation of Y362 may promote astral MT symmetry and the efficiency of dynein in maintaining the position of the SPBs in the mother and bud compartments. The 2-fold increase in the number of astral MTs associated with the new SPB, which frequently lacks astral MTs in wild-type cells, opens the possibility that phosphorylation of Y362 may contribute to γ -TuRC activation, which has previously been shown to increase nucleation by ~2-fold¹⁵. Given the evolutionary conservation of Y362 across eukaryotes, phosphorylation could be part of a general mechanism for control of microtubule number.

Methods

Strains, Plasmids, Genetic Manipulation and Growing Conditions. All yeast strains are derivatives of BY4741⁶² and are listed in Supplemental Table I. All plasmids used in this study are listed in Supplemental Table II. Point mutations (Y362E, Y445D, etc.) were generated on plasmids using USERTM cloning⁶³ followed by sequencing to confirm error free introduction of the desired mutation. PCR-based methods were used to integrate point mutations and fluorophore tags into the native gene locus on the chromosome under their endogenous promoters⁶⁴. Venus-Tub1 was made by integrating pHis3p::Venus-Tub1 + 3'UTR::His3 (gift from Wei-Lih Lee, Addgene plasmid # 50656)^{65,66} into the knocked out his3 Δ 1 locus of BY4741, with the Venus-Tub1 fusion expressed under the native HIS3 promoter. Yeast strains were grown in YEPD medium⁶⁷ at 25 °C unless otherwise stated. For fluorescence live-cell microscopy, cells were grown in synthetic complete (SC) medium⁶⁸. Bacterial cells used from cloning were grown at 37 °C in LB medium supplemented with 100 μ g/mL of carbenicillin.

Live cell microscopy. Yeast cells expressing Spc42-Cerulean were grown to log phase in SC medium supplemented with 2 mM of ascorbate, and imaged at 25 °C on a custom-built spinning-disk confocal microscope as previously described¹⁹. Briefly, the following components were installed on a Leica DM6000 inverted microscope: a 100x/1.46 numerical aperture plan apochromatic objective, an XY stage with a Z top piezo (Applied Scientific Instrumentation), a Borealis head (a Quorum conversion of a Yokogawa QLC-100). Solid state lasers (446 and 515 nm) with an emission filter wheel were used for multicolor imaging. A Hamamatsu ImagEM EM-CCD camera was used for detection. MetaMorph (Molecular Devices) was used for image acquisition. Images were collected in a streaming regime as Z-stacks (200 or 300 nm Z-steps across 31 or 30 focal planes, respectively) with an integration time of 50 ms per focal plane. For spindle dynamics and alignment studies, cells were imaged over

ten minutes with a ten second time step between stack acquisitions. For imaging astral MTs in live cells, strains containing Venus-Tub1 were imaged over five minutes with five second time step between stack acquisitions (the Spc42-Cerulean pole reporter was collected with ten second time steps in these strains).

Analysis of spindle stability, alignment, positioning and orientation. Pole-tracking was implemented using MatLab (Mathworks) as previously described¹⁹. Briefly, SPBs were fit to 3-dimensional gaussians and tracked by nearest neighbor analysis. Spindle stability was measured by computing the standard deviation of the instantaneous spindle lengths (referred to as spindle fluctuations) of each cell over the ten-minute time course. For spindle positioning and alignment, the bud neck was defined by manually drawing a line through the neck in the brightfield image. Spindle positioning at the bud neck was measured by calculating the mean distance between the SPB proximal to the bud and the bud neck. This distance was normalized to the length of the mother to adjust for minor differences in the size of the mother compartment. One-dimensionally projected spindle length was calculated by projecting the SPB coordinates onto the mother-daughter axis, perpendicular to the bud neck plane. Spindle orientation was assessed by first assigning the SPBs as either old or new, based on the mean integrated intensity of Spc42-Cerulean over the ten minute time course, with the brighter SPB identified as the old SPB¹⁹. A spindle was considered mis-oriented if the SPB proximal to the bud neck had a lower mean integrated intensity (i.e. was the ‘new’ SPB) than the distal pole. Spindle alignment heatmaps were generated first as bivariate histograms of 30×30 bins and then smoothed with bicubic interpolation to give 180×180 bins. The color indicates the normalized frequency of data points in each bin across all analyzed cells; the maximum normalized frequency (dark red) indicates all bins with a normalized frequency ≥ 0.015 .

Analysis of astral MTs. Wild-type and γ tub-Y362E cells with astral MTs labeled using Venus-Tub1 were analyzed using Fiji⁶⁹. Astral MTs projecting from each SPB (labeled with Spc42-Cerulean) were detected in maximum projections and counted manually in all time points (61 time points per cell over five minutes, with a time step of five seconds). Astral MTs were only counted once they were resolvable from the central spindle and could be observed for at least two-time points. This dataset was used to compute the mean number of astral MTs per spindle, the mean number of astral MT per SPB, and the number of time points where both SPBs had at least one astral MT during the five-minute acquisition. Intensity of astral MTs was not considered, i.e. we did not discriminate between bundled astral MTs which would appear brighter than a single astral MT, therefore, these data may underestimate the number of astral MTs per spindle/SPB.

Statistics used for Image Analysis. Distributions were tested for normality using a one-sample Kolmogorov-Smirnov test. To test for differences in spindle fluctuations, the variance of changes in spindle length (i.e. between two neighboring time points) was assessed between strains using a Bartlett’s test. Distributions for normalized mean distance from the neck were assessed using the Kruskal-Wallis test followed by a Dunn-Sidak correction. Distributions for the mean number of astral MTs per spindle and for the percentage of total time both poles had astral MTs were assessed for differences using the Wilcoxon rank sum test/Mann-Whitney U-test.

Synthetic Genetic Array. Strains undergoing the SGA process were iteratively grown to select for double mutants using previously described media²⁷ with the aid of a Beckman Coulter Biomek robot. In order to measure the growth rates, an additional robotics platform based on Beckman Coulter’s robotic Orca Arm photographs each final selection plate every two hours for 72 hours.

SGA Image Processing. After data acquisition, the colony densities were extracted from each image as the integrated intensity. To maximize colony detection, a computationally generated grid was overlaid on each plate, where each grid tile contained at most a single colony and was analyzed from the last time point back to the first time point. Each grid tile was analyzed for the presence of a colony. A watershed algorithm was then applied to separate the colony from the background, and density was measured as the integrated intensity over the background of these pixels.

To generate a grid which does not intersect a colony, we first identified colonies using a coarse-grained method based on the circular Hough transform. Since the colonies are pinned in a regular pattern, circular objects that are either too close or too far from one another are removed. The grid lines are fit to these objects such that they do not intersect with the objects and follow the regular pattern of the pin tool resulting in grid tiles containing at most one colony. When an insufficient number of objects was found for grid fitting (less than 100), the grid lines from the later time point were used.

In order to measure the fitness of a colony, the densities were fit to a Gompertz growth equation of the form:

$$Density (time) = A * \exp(B * \exp(-GR * time)) \quad (1)$$

where A is the maximum density of the colony, B is proportional to the initial size at time 0, \exp is the exponential function with base e , GR is the growth rate and $time$ is the elapsed time since the first data point. Here, the growth rate parameter is akin to the doubling time of a single cell and represents the health of the colony. We then normalized the colony densities such that

$$Density (time) = 1 * \exp(B * \exp(-GR * time)) \quad (2)$$

Then, we applied a double logarithm to transform the Gompertz equation into a simple linear equation:

$$\log(\log(Density(time))) = \log(B) - GR * time \quad (3)$$

which is of the form: $y = b + m * x$. Since the parameter of interest is the growth rate, we re-centered time such that $\log(B) = 0$, giving the equation:

$$\log(\log(\text{Density}(\text{time}')) = -GR * \text{time}' \quad (4)$$

where time' is the shifted time.

GAMER Mathematical Model. We defined the competitive fitness of strain i as: $F_i = GR_i / GR_{WT}$ where GR_i is the growth rate of strain i and GR_{WT} is the growth rate of a wild-type reference. A true genetic interaction is inferred when the fitness of the double mutant is significantly different from its expected fitness (defined as the product of the fitness of the individual mutations)^{33,70–72}:

$$F_{ij} = F_i * F_j \quad (5)$$

where F_{ij} is the fitness of the double mutant with mutations i and j .

This definition of the expected fitness of the double mutant is appropriately modeled by a single linear mixed-effects model. This allows us to model the growth rates of each colony of the four genotypes (WT, i , j , ij) using two categorical variables. The only assumption of the model is that all the yeast mutants we screened are derived from a common background strain. This allowed us to assume that any observable growth defects in the mutants (both the single and double mutants) can be attributed to the mutation(s).

For the single mutant i , the growth rate was modeled as: $GR_i = GR_{WT} + d_i$, where d_i is the measurable defect in the growth rate associated to the mutation relative to the common background strain. In the case of the double mutant, the growth rate was modelled as $GR_{ij} = GR_{WT} + d_i + d_j + d_{ij}$, where d_{ij} is the measurable growth defect present only in the double mutant. The expected value of d_{ij} can be determined by substituting the fitness terms in the expected fitness equation with the growth rate terms:

$$\frac{GR_{ij}}{GR_{WT}} = \frac{GR_i}{GR_{WT}} * \frac{GR_j}{GR_{WT}} \quad (6)$$

$$GR_{ij} = \frac{GR_i * GR_j}{GR_{WT}} \quad (7)$$

$$GR_{WT} + d_i + d_j + d_{ij} = \frac{(GR_{WT} + d_i) * (GR_{WT} + d_j)}{GR_{WT}} \quad (8)$$

$$GR_{WT}^2 + GR_{WT} * d_i + GR_{WT} * d_j + GR_{WT} * d_{ij} = GR_{WT}^2 + GR_{WT} * d_i + GR_{WT} * d_j + d_i * d_j \quad (9)$$

$$GR_{WT} * d_{ij} = d_i * d_j \quad (10)$$

$$d_{ij} = \frac{d_i * d_j}{GR_{WT}} \quad (11)$$

We therefore find the expected value for the defect to be:

$$d_{ij} = \frac{d_i * d_j}{GR_{WT}} \quad (12)$$

From this model, a genetic interaction is inferred between the two mutations when the experimentally measured value for d_{ij} is significantly different from the expected value. The GAMER scores were calculated as:

$$\text{GAMER score} = d_{ij, \text{expected}} - d_{ij, \text{observed}} \quad (13)$$

To calculate p-values, we bootstrap the model 20,000 times and calculate the probability of observing a more extreme value than the expected d_{ij} . Finally, we correct the p-values for multiple hypothesis testing by the false discovery rate.

Code and data availability. All strains, code, data and analysis is available upon request.

References

1. Oakley, C. E. & Oakley, B. R. Identification of γ -tubulin, a new member of the tubulin superfamily encoded by mipA gene of *Aspergillus nidulans*. *Nature* **338**, 662–664 (1989).
2. Oakley, B. R., Oakley, C. E., Yoon, Y. & Jung, M. K. γ -Tubulin is a component of the spindle pole body that is essential for microtubule function in *Aspergillus nidulans*. *Cell* **61**, 1289–1301 (1990).
3. Stearns, T., Evans, L. & Kirschner, M. γ -Tubulin is a highly conserved component of the centrosome. *Cell* **65**, 825–836 (1991).
4. Zheng, Y., Jung, M. K. & Oakley, B. R. γ -Tubulin is present in *Drosophila melanogaster* and *Homo sapiens* and is associated with the centrosome. *Cell* **65**, 817–823 (1991).

5. Horio, T. *et al.* The fission yeast gamma-tubulin is essential for mitosis and is localized at microtubule organizing centers. *Journal of Cell Science* **99**, 693–700 (1991).
6. Joshi, H. C., Palacios, M. J., McNamara, L. & Cleveland, D. W. γ -Tubulin is a centrosomal protein required for cell cycle-dependent microtubule nucleation. *Nature* **356**, 80–83 (1992).
7. Zheng, Y., Wong, M., Alberts, B. & Mitchison, T. Nucleation of microtubule assembly by a gamma-tubulin-containing ring complex. *Nature* **378**, 578–583 (1995).
8. Sobel, S. G. & Snyder, M. A highly divergent gamma-tubulin gene is essential for cell growth and proper microtubule organization in *Saccharomyces cerevisiae*. *The Journal of Cell Biology* **131**, 1775–1788 (1995).
9. Geissler, S. *et al.* The spindle pole body component Spc98p interacts with the gamma-tubulin-like Tub4p of *Saccharomyces cerevisiae* at the sites of microtubule attachment. *The EMBO Journal* **15**, 3899 (1996).
10. Knop, M., Pereira, G., Geissler, S., Grein, K. & Schiebel, E. The spindle pole body component Spc97p interacts with the γ -tubulin of *Saccharomyces cerevisiae* and functions in microtubule organization and spindle pole body duplication. *The EMBO Journal* **16**, 1550–1564 (1997).
11. Jaspersen, S. L. & Winey, M. The budding yeast spindle pole body: structure, duplication, and function. *Annu. Rev. Cell Dev. Biol.* **20**, 1–28 (2004).
12. Byers, B. & Goetsch, L. Behavior of spindles and spindle plaques in the cell cycle and conjugation of *Saccharomyces cerevisiae*. *Journal of Bacteriology* **124**, 511–523 (1975).
13. Knop, M. & Schiebel, E. Receptors determine the cellular localization of a γ -tubulin complex and thereby the site of microtubule formation. *The EMBO Journal* **17**, 3952–3967 (1998).
14. Knop, M. & Schiebel, E. Spc98p and Spc97p of the yeast γ -tubulin complex mediate binding to the spindle pole body via their interaction with Spc110p. *The EMBO Journal* **16**, 6985–6995 (1997).
15. Kollman, J. M. *et al.* Ring closure activates yeast γ TuRC for species-specific microtubule nucleation. *Nat. Struct. Mol. Biol.* **22**, 132–137 (2015).
16. Keck, J. M. *et al.* A cell cycle phosphoproteome of the yeast centrosome. *Science* **332**, 1557–1561 (2011).
17. Vogel, J. *et al.* Phosphorylation of gamma-tubulin regulates microtubule organization in budding yeast. *Dev. Cell* **1**, 621–631 (2001).
18. Bloom, J. & Cross, F. R. Multiple levels of cyclin specificity in cell-cycle control. *Nat. Rev. Mol. Cell Biol.* **8**, 149–160 (2007).
19. Nazarova, E. *et al.* Distinct roles for antiparallel microtubule pairing and overlap during early spindle assembly. *Mol Biol Cell* **24**, 3238–3250, <https://doi.org/10.1091/mbc.E13-05-0232> (2013).
20. Stirling, P. C. *et al.* The complete spectrum of yeast chromosome instability genes identifies candidate CIN cancer genes and functional roles for ASTRA complex components. *PLoS Genet* **7**, e1002057 (2011).
21. Li, R. & Murray, A. W. Feedback control of mitosis in budding yeast. *Cell* **66**, 519–531 (1991).
22. Hardwick, K. G. *et al.* Lesions in many different spindle components activate the spindle checkpoint in the budding yeast *Saccharomyces cerevisiae*. *Genetics* **152**, 509–518 (1999).
23. Vogel, J. & Snyder, M. The carboxy terminus of Tub4p is required for gamma-tubulin function in budding yeast. *Journal of Cell Science* (2000).
24. Cuschieri, L., Miller, R. & Vogel, J. Gamma-tubulin is required for proper recruitment and assembly of Kar9-Bim1 complexes in budding yeast. *Mol. Biol. Cell* **17**, 4420–4434 (2006).
25. Braberg, H. *et al.* From structure to systems: high-resolution, quantitative genetic analysis of RNA polymerase II. *Cell* **154**, 775–788 (2013).
26. Winzeler, E. A. *et al.* Functional characterization of the *S. cerevisiae* genome by gene deletion and parallel analysis. *science* **285**, 901–906 (1999).
27. Baryshnikova, A. *et al.* Synthetic genetic array (SGA) analysis in *Saccharomyces cerevisiae* and *Schizosaccharomyces pombe*. *Methods in ...* **470**, 145–179 (2010).
28. Tong, A. *et al.* Systematic genetic analysis with ordered arrays of yeast deletion mutants. *Science* **294**, 2364–2368 (2001).
29. Costanzo, M. *et al.* The genetic landscape of a cell. *Science* **327**, 425–431 (2010).
30. Turney, D., de los Santos, T. & Hollingsworth, N. M. Does chromosome size affect map distance and genetic interference in budding yeast? *Genetics* **168**, 2421–2424 (2004).
31. Kaback, D. B., Steensma, H. Y. & De Jonge, P. Enhanced meiotic recombination on the smallest chromosome of *Saccharomyces cerevisiae*. *Proceedings of the National Academy of Sciences* **86**, 3694–3698 (1989).
32. Zhu, Y. & Kuang, D. Construction of the physical map of yeast (*Saccharomyces cerevisiae*) chromosome V. *Cell Research* **2**, 25–34 (1992).
33. Baryshnikova, A. *et al.* Quantitative analysis of fitness and genetic interactions in yeast on a genome scale. *Nat. Methods* **7**, 1017–1024 (2010).
34. Schuyler, S. C., Liu, J. Y. & Pellman, D. The molecular function of Ase1p. *J Cell Biol* **160**, 517–528 (2003).
35. Zeng, X. *et al.* Slk19p is a centromere protein that functions to stabilize mitotic spindles. *The Journal of Cell Biology* **146**, 415–425 (1999).
36. Manning, B. D., Barrett, J. G., Wallace, J. A., Granok, H. & Snyder, M. Differential regulation of the Kar3p kinesin-related protein by two associated proteins, Cik1p and Vik1p. *The Journal of Cell Biology* **144**, 1219–1233 (1999).
37. Allingham, J. S., Sproul, L. R., Rayment, I. & Gilbert, S. P. Vik1 modulates microtubule-Kar3 interactions through a motor domain that lacks an active site. *Cell* **128**, 1161–1172 (2007).
38. Sproul, L. R., Anderson, D. J., Mackey, A. T., Saunders, W. S. & Gilbert, S. P. Cik1 targets the minus-end kinesin depolymerase kar3 to microtubule plus ends. *Current Biology* **15**, 1420–1427 (2005).
39. D'Aquino, K. E. *et al.* The protein kinase Kin4 inhibits exit from mitosis in response to spindle position defects. *Molecular Cell* **19**, 223–234 (2005).
40. Pereira, G. & Schiebel, E. Kin4 kinase delays mitotic exit in response to spindle alignment defects. *Molecular Cell* **19**, 209–221 (2005).
41. Ear, P. H. *et al.* Dissection of Cdk1-cyclin complexes *in vivo*. *Proceedings of the National Academy of Sciences* (2013).
42. Pereira, G., Tanaka, T., Nasmyth, K. & Schiebel, E. Modes of spindle pole body inheritance and segregation of the Bfa1p-Bub2p checkpoint protein complex. *EMBO J.* **20**, 6359–6370 (2001).
43. Rauch, A., Nazarova, E. & Vogel, J. Analysis of microtubules in budding yeast. *Methods Cell Biol.* **97**, 277–306 (2010).
44. Kusch, J., Meyer, A., Snyder, M. P. & Barral, Y. Microtubule capture by the cleavage apparatus is required for proper spindle positioning in yeast. *Genes & Development* **16**, 1627–1639 (2002).
45. Palmer, R., Sullivan, D., Huffaker, T. & Koshland, D. Role of astral microtubules and actin in spindle orientation and migration in the budding yeast, *Saccharomyces cerevisiae*. *The Journal of Cell Biology* **119**, 583–593 (1992).
46. Segal, M. & Bloom, K. Control of spindle polarity and orientation in *Saccharomyces cerevisiae*. *Trends in Cell Biology* (2001).
47. Theesfeld, C. L., Irazoqui, J. E., Bloom, K. & Lew, D. J. The role of actin in spindle orientation changes during the *Saccharomyces cerevisiae* cell cycle. *J Cell Biol* **146**, 1019–1032 (1999).
48. Gupta, M. L. *et al.* β -Tubulin C354 mutations that severely decrease microtubule dynamics do not prevent nuclear migration in yeast. *Molecular Biology of the Cell* **13**, 2919–2932 (2002).
49. Liakopoulos, D., Kusch, J., Grava, S., Vogel, J. & Barral, Y. Asymmetric Loading of Kar9 onto Spindle Poles and Microtubules Ensures Proper Spindle Alignment. *Cell* (2003).

50. Maekawa, H., Usui, T., Knop, M. & Schiebel, E. Yeast Cdk1 translocates to the plus end of cytoplasmic microtubules to regulate bud cortex interactions. *EMBO J.* **22**, 438–449 (2003).
51. Shaw, S. L., Yeh, E., Maddox, P., Salmon, E. D. & Bloom, K. Astral microtubule dynamics in yeast: a microtubule-based searching mechanism for spindle orientation and nuclear migration into the bud. *The Journal of cell biology* **139**, 985–994 (1997).
52. Addinall, S. G. *et al.* Quantitative fitness analysis shows that NMD proteins and many other protein complexes suppress or enhance distinct telomere cap defects. *PLoS Genet.* **7**, e1001362 (2011).
53. Li, Y.-Y., Yeh, E., Hays, T. & Bloom, K. Disruption of mitotic spindle orientation in a yeast dynein mutant. *Proceedings of the National Academy of Sciences* **90**, 10096–10100 (1993).
54. Miller, R. K. & Rose, M. D. Kar9p is a novel cortical protein required for cytoplasmic microtubule orientation in yeast. *J Cell Biol* **140**, 377–390 (1998).
55. Adames, N. R. & Cooper, J. A. Microtubule interactions with the cell cortex causing nuclear movements in *Saccharomyces cerevisiae*. *J Cell Biol* **149**, 863–874 (2000).
56. Yin, H., Pruyne, D., Huffaker, T. C. & Bretscher, A. Myosin V orientates the mitotic spindle in yeast. *Nature* **406**, 1013–1015, <https://doi.org/10.1038/35023024> (2000).
57. Hotz, M. *et al.* Spindle pole bodies exploit the mitotic exit network in metaphase to drive their age-dependent segregation. *Cell* **148**, 958–972 (2012).
58. Grava, S., Schaerer, F., Faty, M., Philippsen, P. & Barral, Y. Asymmetric recruitment of dynein to spindle poles and microtubules promotes proper spindle orientation in yeast. *Developmental cell* **10**, 425–439 (2006).
59. Yeh, E. *et al.* Dynamic positioning of mitotic spindles in yeast: role of microtubule motors and cortical determinants. *Molecular biology of the cell* **11**, 3949–3961 (2000).
60. Choy, J. S. *et al.* Genome-wide haploinsufficiency screen reveals a novel role for γ -TuSC in spindle organization and genome stability. *Molecular biology of the cell* **24**, 2753–2763 (2013).
61. Lengefeld, J., Hotz, M., Rollins, M., Baetz, K. & Barral, Y. Budding yeast Wee1 distinguishes spindle pole bodies to encode their pattern of age-dependent segregation. *Nature Cell biology* (2017, in press).
62. Brachmann, C. B. *et al.* Designer deletion strains derived from *Saccharomyces cerevisiae* S288C: a useful set of strains and plasmids for PCR-mediated gene disruption and other applications. *Yeast-Chichester* **14**, 115–132 (1998).
63. Bitinaite, J. *et al.* USERTM friendly DNA engineering and cloning method by uracil excision. *Nucleic acids research* **35**, 1992–2002 (2007).
64. Gietz, R. D. & Schiestl, R. H. High-efficiency yeast transformation using the LiAc/SS carrier DNA/PEG method. *Nat Protoc* **2**, 31–34, <https://doi.org/10.1038/nprot.2007.13> (2007).
65. Markus, S. M., Omer, S., Baranowski, K. & Lee, W. L. Improved plasmids for fluorescent protein tagging of microtubules in *Saccharomyces cerevisiae*. *Traffic* **16**, 773–786 (2015).
66. Janke, C. *et al.* A versatile toolbox for PCR-based tagging of yeast genes: new fluorescent proteins, more markers and promoter substitution cassettes. *Yeast* **21**, 947–962 (2004).
67. Sherman, F. [1] Getting started with yeast. *Methods in enzymology* **194**, 3–21 (1991).
68. Rines, D. R., Thomann, D., Dorn, J. F., Goodwin, P. & Sorger, P. K. Live cell imaging of yeast. *Cold Spring Harbor Protocols* **2011**, pdb.top065482 (2011).
69. Schindelin, J. *et al.* Fiji: an open-source platform for biological-image analysis. *Nature methods* **9**, 676–682 (2012).
70. Elena, S. & Lenski, R. Test of synergistic interactions among deleterious mutations in bacteria. *Nature* **390**, 395–398 (1997).
71. Phillips, P. C., Otto, S. P. & Whitlock, M. C. Beyond the average. 20–40 (2000).
72. Collins, S. R., Roguev, A. & Krogan, N. J. Chapter 11 Quantitative Genetic Interaction Mapping Using the E-MAP Approach. **470**, 205–231 (2010).

Acknowledgements

The authors thank current and past members of the Vogel lab for stimulating discussions during this work, Brian Leung (McGill Biology) for input during the development of GAMER, and Elke Küster-Schöck and Guillaume Lesage for robotics support.

Author Contributions

J.V. directed the research; K.S. constructed strains and performed genetic analysis and live cell microscopy and analyzed image data; E.Y. developed the GAMER method, analyzed GAMER datasets and implemented tracking methods used for image analysis; S.K. performed quality control for strains and arrays used for S.G.A. and oversaw S.G.A. experiments; A.L. contributed to the analysis of spindle alignment; A.D. assisted with strain constructions and genetic analysis; D.G. assisted in development of GAMER image processing steps; K.S., E.Y., A.L. and J.V. prepared the figures; A.L. edited the manuscript and K.S., E.Y. and J.V. wrote the manuscript. All authors reviewed the manuscript.

Additional Information

Supplementary information accompanies this paper at <https://doi.org/10.1038/s41598-017-11789-7>

Competing Interests: The authors declare that they have no competing interests.

Change History: A correction to this article has been published and is linked from the HTML version of this paper. The error has not been fixed in the paper.

Publisher's note: Springer Nature remains neutral with regard to jurisdictional claims in published maps and institutional affiliations.



Open Access This article is licensed under a Creative Commons Attribution 4.0 International License, which permits use, sharing, adaptation, distribution and reproduction in any medium or format, as long as you give appropriate credit to the original author(s) and the source, provide a link to the Creative Commons license, and indicate if changes were made. The images or other third party material in this article are included in the article's Creative Commons license, unless indicated otherwise in a credit line to the material. If material is not included in the article's Creative Commons license and your intended use is not permitted by statutory regulation or exceeds the permitted use, you will need to obtain permission directly from the copyright holder. To view a copy of this license, visit <http://creativecommons.org/licenses/by/4.0/>.